

Allosteric switch regulates protein–protein binding through collective motion

Colin A. Smith^{a,b,1}, David Ban^{b,c}, Supriya Pratihar^b, Karin Giller^b, Maria Paulat^b, Stefan Becker^b, Christian Griesinger^{b,1}, Donghan Lee^{b,c,1}, and Bert L. de Groot^{a,1}

^aDepartment for Theoretical and Computational Biophysics, Max Planck Institute for Biophysical Chemistry, 37077 Goettingen, Germany; ^bDepartment for NMR-Based Structural Biology, Max Planck Institute for Biophysical Chemistry, 37077 Goettingen, Germany; and ^cDepartment of Medicine, James Graham Brown Cancer Center, University of Louisville, Louisville, KY 40202

Edited by David Baker, University of Washington, Seattle, WA, and approved February 9, 2016 (received for review October 5, 2015)

Many biological processes depend on allosteric communication between different parts of a protein, but the role of internal protein motion in propagating signals through the structure remains largely unknown. Through an experimental and computational analysis of the ground state dynamics in ubiquitin, we identify a collective global motion that is specifically linked to a conformational switch distant from the binding interface. This allosteric coupling is also present in crystal structures and is found to facilitate multispecificity, particularly binding to the ubiquitin-specific protease (USP) family of deubiquitinases. The collective motion that enables this allosteric communication does not affect binding through localized changes but, instead, depends on expansion and contraction of the entire protein domain. The characterization of these collective motions represents a promising avenue for finding and manipulating allosteric networks.

allostery | protein dynamics | concerted motion | relaxation dispersion | nuclear magnetic resonance

Intermolecular interactions are one of the key mechanisms by which proteins mediate their biological functions. For many proteins, these interactions are enhanced or suppressed by allosteric networks that couple distant regions together (1). The mechanisms by which these networks function are just starting to be understood (2–4), and many of the important details have yet to be uncovered. In particular, the role of intrinsic protein motion and kinetics remains particularly poorly characterized. A number of structural ensembles representing ubiquitin motion have been recently proposed (5–9). Additionally, it has been suggested that through motion at the binding interface, its free state visits the same conformations found in complex with its many binding partners (5, 10). However, it remains an unanswered question if the dynamics that enable this multispecificity are only clustered around the canonical binding interface or whether this motion is allosterically coupled to the rest of the protein, especially given the presence of motion at distal sites (11).

Results

To answer this question and to provide a detailed structural picture of the underlying mechanism, we applied recently developed high-power relaxation dispersion (RD) experiments (12, 13) to both the backbone amide proton (¹H^N) and nitrogen (¹⁵N) nuclei of ubiquitin. This survey yielded a nearly twofold increase in the number of nuclei where RD had been previously observed (11–14) (from 17 to 31; Fig. 1*A* and Fig. S1). When fit individually, the full set of backbone and side-chain nuclei shows a consistent time scale of motion [exchange lifetime (τ_{ex}) = 55 μ s; Fig. 1*B*]. Furthermore, the nuclei showing exchange are spread throughout the structure (Fig. 1*C*). Put together, these data suggest that the motions are not independent but share a common molecular mechanism.

To determine whether the RD data could be modeled using a single collective motion, we developed a computational method to take a set of molecular dynamics (MD) simulations (10) and derive an optimized linear mode of motion that best explains the RD data (Fig. S2). For all types of nuclei, the resulting collective mode, termed the “RD fit MD mode,” predicts the RD data

much better than expected for a random model (Fig. 1*D* and Figs. S3 and S4). The RD fit MD mode therefore represents a detailed structural model for the reaction coordinate along which much of the microsecond motion takes place (Fig. 1*E*). This mode is one of the first atomic models for a fast exchange transition in the ground state, whereas other models of motions in the microsecond range have involved the interconversion between a ground state and excited states having distinct chemical shifts (15, 16). A clustering analysis of the RD fit MD mode shows that the motion can be separated into several different regions that maintain a relatively stable internal structure (Fig. 1*F*). Two adjacent regions twist in opposite directions against one another, whereas another region moves in a rocking motion.

Located at the intersection of these regions, the peptide bond between D52 and G53 undergoes a discrete flip in orientation, unlike the relatively continuous motion observed elsewhere. This flip is also observed if experimental data for residues within 5 Å of D52 and G53 are excluded from fitting the optimized mode. Both orientations of this peptide bond have been observed crystallographically (17, 18) (Fig. 2). In addition, a previous study using mutagenesis and extreme pH values suggested that rotation of this peptide bond may explain the microsecond motion observed in two nearby residues (19). Microsecond motions in this region have also been observed with heteronuclear double-resonance (20) and solid-state RD (21) experiments. Furthermore, in the 100-ns simulations used for modeling the RD fit MD mode, peptide flipping was the structural feature with the slowest time scale, with flips occurring in 21 of 170 independent simulations (Fig. S5). It is also observed in a recently published 1-ms ubiquitin simulation (22) (Fig. S6). Taken together, the flip

Significance

Within biological molecules, a change in shape at one site affecting a distant site is called allostery, and is a process critical for sustaining life. At the atomic level, the means of communication is often not well understood. We identify a previously unidentified way for allostery to occur through collective motion of an entire protein structure. Together with newly developed computational algorithms, we determine atomic structures representing this previously invisible allosteric motion. This allosteric network is shown to be an intrinsic property of the protein and important for enabling binding to different protein partners. The nature of this motion, along with the tools we developed to detect it, should prove invaluable for understanding living organisms and developing new therapeutics.

Author contributions: C.A.S., C.G., D.L., and B.L.d.G. designed research; C.A.S., D.B., and S.P. performed research; C.A.S., K.G., M.P., S.B., and D.L. contributed new reagents/analytic tools; C.A.S. and D.B. analyzed data; and C.A.S., D.B., C.G., D.L., and B.L.d.G. wrote the paper.

The authors declare no conflict of interest.

This article is a PNAS Direct Submission.

¹To whom correspondence may be addressed. Email: colin.smith@mpibpc.mpg.de, cigr@nmr.mpiibpc.mpg.de, donghan.lee@louisville.edu, or bgroot@gwdg.de.

This article contains supporting information online at www.pnas.org/lookup/suppl/doi:10.1073/pnas.1519609113/-DCSupplemental.

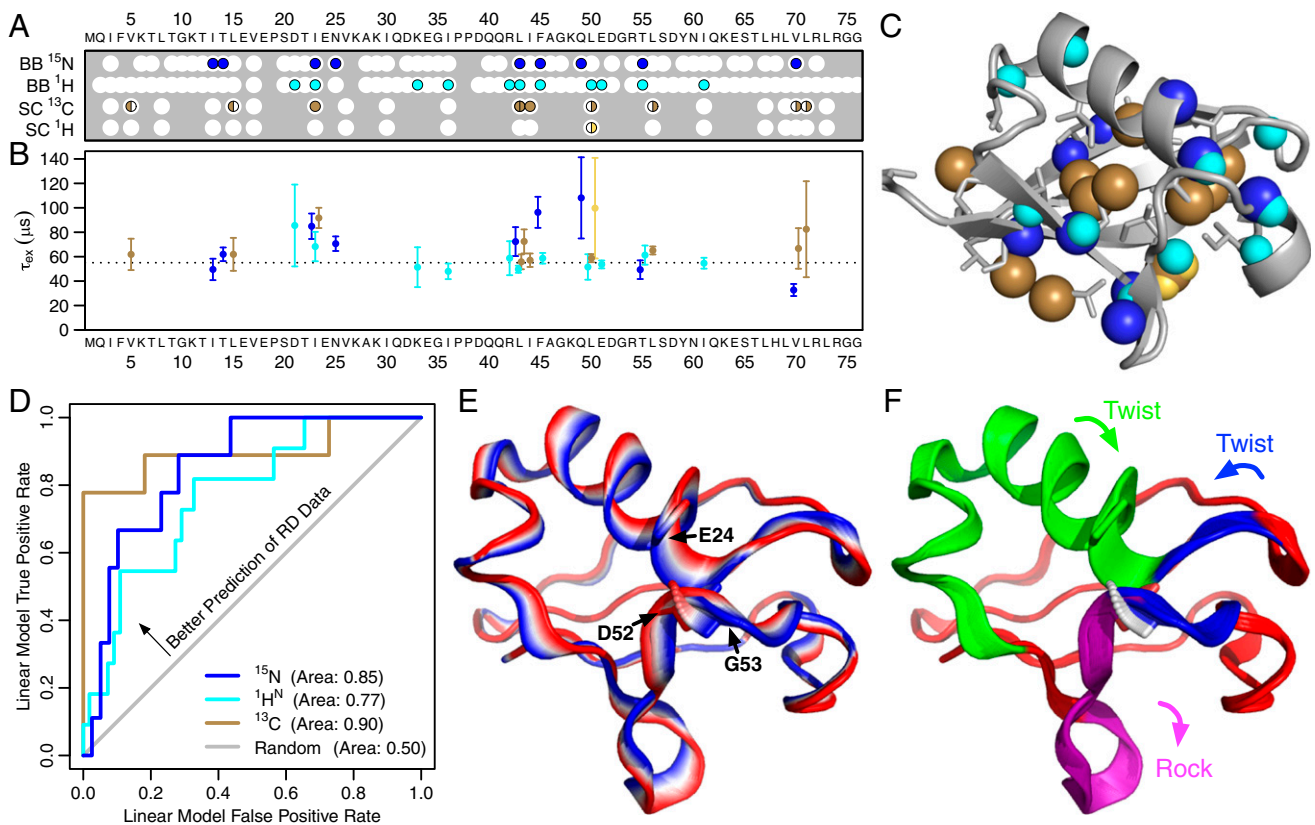


Fig. 1. Single collective mode explains the majority of the RD data. (A) Thirty-one different nuclei show statistically significant RD at 277 K and are spread across the primary sequence of ubiquitin. White circles indicate residues for which measuring an RD curve was possible. Where two labeled methyl groups were present in the same residue, shaded semicircles indicate the respective methyl(s) showing dispersion. (B) When fit individually, most nuclei show a similar exchange lifetime (τ_{ex}) that is consistent with the globally fit value of 55 μ s (dotted line). (C) Nuclei showing RD are distributed throughout the structure, suggesting concerted motion of the whole structure. (D) ROC curves show that an optimized collective mode can predict a significant fraction of the ¹⁵N, ¹H, and ¹³C RD data ($P = 0.027$; Fig. S3). The straight gray line indicates a random prediction. (E) Interpolation of the backbone from one extreme of the concerted motion vector (blue) to the other (red). The rotating peptide bond between Asp 52 and Gly 53 is shown with a stick representation, along with the α -C β vector of Glu 24. (F) Optimized motional mode contains several semirigid substructures, each indicated by a different color (Movie S1).

of the D52-G53 peptide bond emerges as one of the key parts of the concerted motion.

When the NH group of the D52-G53 peptide bond is pointed outward into the solvent (the “NH-out” state; Fig. 2A), the ¹H nuclei of E24 and G53 are hydrogen-bonded with neutral species (namely, water or an amide carbonyl group). By contrast, when the NH group points in toward the protein (the “NH-in” state; Fig. 2B), both nuclei make hydrogen bonds with the negatively charged side chain of E24. The chemical shift difference between these states should be quite large and result in significant RD. At 277 K, where the initial data were collected, the E24 and G53 amide proton peaks are severely broadened and undetectable. At 308 K, the peaks are visible and our high-power RD experiments (13) indeed reveal significant RD for both nuclei. Their time scales exactly coincide with other residues exhibiting RD at both 277 K and 308 K (Fig. 2C and Fig. S7). Furthermore, the chemical shift variance (Φ_{ex}) for these two nuclei is at least an order of magnitude greater than any others we observed (Fig. 2D), in agreement with the expected large chemical shift change.

To investigate the necessity of the peptide flip for this collective ubiquitin motion, we used two mutants, E24A and G53A, that have been shown to inhibit the NH-in state (19). In the presence of these mutants, ¹H RD is either abolished or significantly attenuated (at least by a factor of 10) at all but one residue (Fig. 2E and Fig. S8). This observation suggests that although at least two processes occur on the microsecond time scale [peptide flipping and motion around I36 (22–24)], peptide flipping is directly coupled with the majority of the conformational

fluctuation throughout the structure. This finding is further supported by the temperature dependence of ¹H RD, in which the majority of residues show profiles that coincide with E24 and G53 (Fig. S9). Finally, the chemical shift differences between the WT and mutant proteins almost entirely explain the RD magnitudes observed at all but one of the nuclei (Fig. 2F and Fig. S10). In addition to confirming the linkage between the peptide flip and the concerted motion, a comparison of the mutant chemical shifts and Φ_{ex} values show that the population of each state is \sim 50% (Fig. S10), indicating that the motion is occurring in the ground state of the protein.

To determine how this collective motion influences binding and other functions of ubiquitin (e.g., presence of different covalent linkages), we performed an extensive structural bioinformatics survey of known ubiquitin crystal structures. Because the peptide bond conformation was the most recognizable feature of the collective mode, we used its conformation as a “marker” for structural discrimination. The most significant relationship we found was the universal association between the NH-in state and binding to the ubiquitin-specific protease (USP) family of deubiquitinases (Fig. S11). This association has been previously noted (18) and is surprising because the peptide bond is at least 6.8 Å from any USP (Fig. 3A).

Given that when free in solution, changes in the peptide bond affect residues throughout ubiquitin, we hypothesized that specific conformations of residues at the USP-ubiquitin binding interface could be allosterically associated with the NH-in state. To test this hypothesis using completely independent data, we

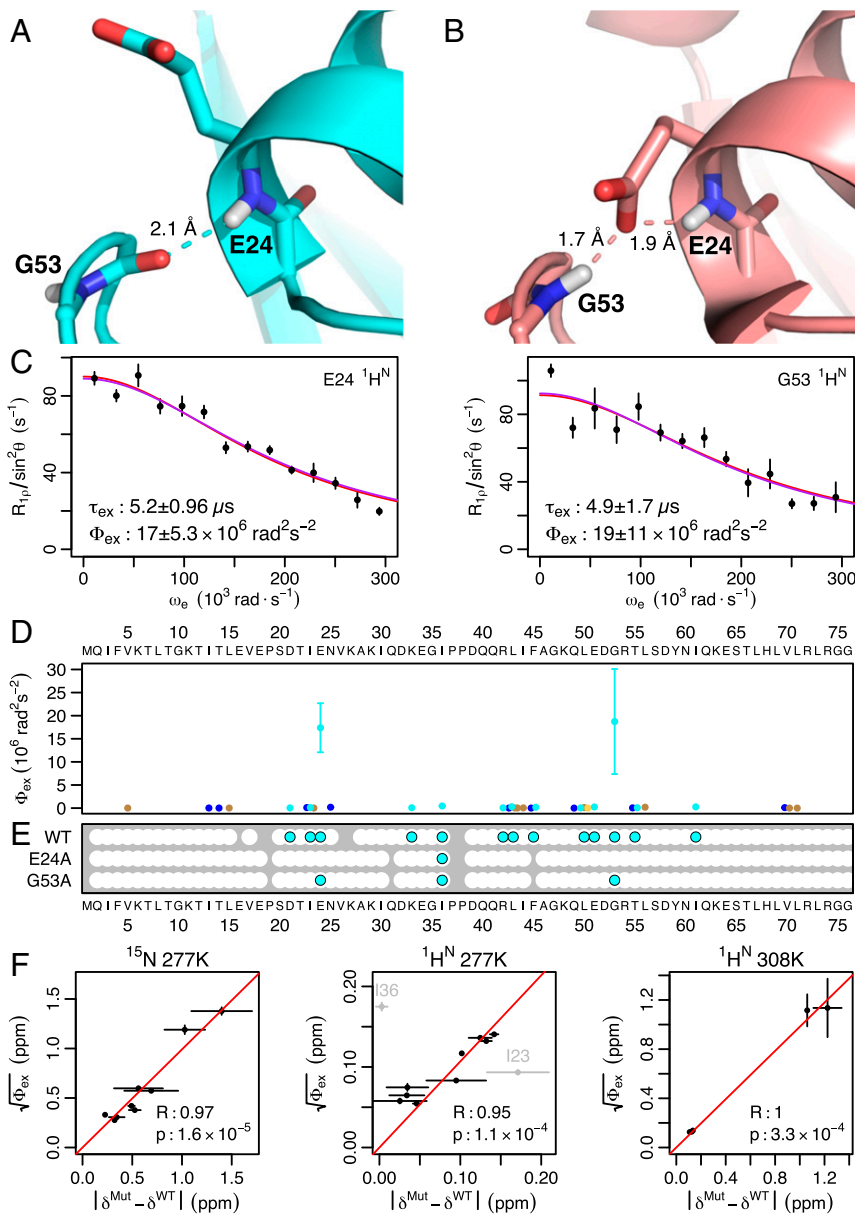


Fig. 2. High-power RD and mutation confirms peptide bond flipping as an integral part of the collective motion. (A) In most crystal structures, the G53 backbone NH points out. (B) In a subset of crystal structures, the G53 NH points in. (C) Although the E24 and G53 NH resonances are invisible at 277 K ($\tau_{ex} \approx 55 \mu\text{s}$), high-power RD at 308 K speeds up the exchange process and shows these two protons exchanging at the same rate as L43, E51, and I61 ($\tau_{ex} \approx 5 \mu\text{s}$; Fig. S7E). Individual fits (red lines) are indistinguishable from a global fit to the five residues (purple lines). (D) Chemical shift variance (Φ_{ex}) for E24 and G53 (at 308 K) is one to two orders of magnitude greater than any other nucleus (at 277 K), in agreement with the large chemical shift difference expected. (E) When either E24 or G53 is mutated to suppress the NH-in state, $^1\text{H}^N$ RD becomes undetectable at nearly all residues except I36. Although the G53A mutant shows some RD at residues 24 and 53, Φ_{ex} values lowered by a factor of 10 or more suggest a 20-fold reduction in the population of the NH-in state (Figs. S7E and S8B). (F) Chemical shift differences between mutant and WT ($|\delta^{Mut} - \delta^{WT}|$) are highly correlated with $\sqrt{\Phi_{ex}}$, confirming coupling between the collective motion and the peptide bond. The red line shows the best fit through the origin. I23 was excluded because of its proximity to the mutations, and I36 was excluded because its motion is independent of the peptide bond.

assembled a set of 217 distinct ubiquitin conformations from 70 high-resolution crystal structures in the Protein Data Bank (PDB). We used partial least squares (PLS) functional mode analysis (FMA) (25, 26) to train a linear model to predict the peptide bond conformation solely from the coordinates of residues that interact with USPs, thus excluding the peptide flip region (Fig. 3B). The ability of the resulting model, termed the “peptide fit PDB mode,” to distinguish NH-in from NH-out states based solely on the binding interface indicates a strong allosteric coupling between opposite sides of the protein (Fig. 3 and Fig. S12). Furthermore, the peptide fit PDB mode shares a number of common features and shows a statistically significant correlation ($P < 0.001$) with the RD fit MD mode (Fig. S13), indicating that the long-distance structural correlations present in crystal structures are similar to the long-distance structural correlations observed in solution.

A visual examination of the model shows that NH-out conformations are associated with subtle expansion of ubiquitin around the binding interface, whereas NH-in conformations are contracted (Fig. 4A). The greatest expansion was 0.95 Å (from NH-in to NH-out), which was observed between the C α atom of residue 35 and the amide nitrogen of residue 49. To determine if

contraction confers an energetic benefit for USP binding, we used Rosetta software to determine whether shifting expanded NH-out conformations to be more NH-in-like relieved atomic overlaps with the USP (or vice versa). There is a clear trend where the expanded NH-out state has significantly more clashes with the USP than the contracted NH-in state (Fig. 4B). Given the relative subtlety of the expansion and contraction, it is somewhat surprising that the USPs do not accommodate binding to the expanded NH-out state. A possible explanation comes from comparison of the conformations of USP with (holo) and without (apo) ubiquitin bound (Fig. 4C). The crystal structures strongly suggest that USPs energetically favor a closed conformation that occludes ubiquitin binding. By adopting a contracted NH-in conformation, ubiquitin reduces the amount of USP opening required for binding. In that way, both proteins appear to adapt their conformations mutually to establish a complementary binding interaction (Fig. 4D). The greater USP structural heterogeneity suggests that it is more flexible than ubiquitin and able to deform more to accommodate binding.

To verify the hypothesis that the orientation of the peptide bond is linked to the contraction/expansion of ubiquitin,

and binding affinity. This observation points toward potential strategies for the rational design of allosteric mutations or ligands.

Methods

Sample Preparation, NMR, and USP2 Inhibition Assays. Protein sample preparation (32), $R_{1\rho}$ (12, 33, 34) and Carr–Purcell–Meiboom–Gill (CPMG) (35–37) experiments, and USP2 inhibition assays (32) were adapted from the cited work. Further details and other data analysis procedures are provided in *SI Methods*.

Predicting RD from MD Snapshots and Principal Component Analysis Eigenvectors. The method we developed was inspired by FMA (25), in which a linear combination of modes from principal component analysis (PCA) is derived that corresponds to some functional property that can be assigned to each structural snapshot. By contrast, our new algorithm was designed to find a combination of PCA modes that, together, produces a collective motion along which only nuclei showing RD vary their chemical shifts (Fig. S2).

Previous MD simulations of ubiquitin as a free monomer (10) were used to approximate the solution state ensemble. For those simulations, 17 starting conformations were taken from distinct structures of ubiquitin in complex with different binding partners. From each starting structure, 10 separate 100-ns simulations were performed in GROMACS 4 with the amber99sb force field. Snapshots were recorded every 10 ps, and the first 10 ns of each simulation was excluded to allow structural relaxation from the bound form.

To estimate whether chemical shifts of individual nuclei would be affected by structural rearrangements, different metrics were used depending on the specific nuclei involved. For backbone amide nitrogens and protons, chemical shifts were predicted using SHFTX+ version 1.07 (38). Because methyl carbon chemical shift predictions have traditionally performed poorly, and because previous results suggested that rotamer effects were the primary source of methyl carbon chemical shift perturbation (13), we used side-chain χ -angles as a proxy for methyl chemical shifts.

The optimization algorithm involved evaluating the ability of many possible linear modes of motion (each representing a hypothetical reaction coordinate) to predict which residues showed RD. Given a hypothetical mode for evaluation and a single MD trajectory, the algorithm first projected all of the snapshots of that trajectory onto the linear mode. From this projection, two subensembles were assembled, one containing snapshots with negative projection values and the other with snapshots having positive projection values. These ensembles represent the two states in an assumed two-state exchange process.

For each of the two subensembles, distributions of chemical shifts or side-chain χ -angles were calculated using kernel density estimation with a Gaussian smoothing function (SDs of 1 ppm, 0.15 ppm, and 5°, respectively, for amide nitrogens, amide protons, and χ -angles). Differences between the distributions for the two states should indicate a probable chemical shift change. To ensure that only statistically significant differences were taken into account, distributions for the 10 independent simulations from each starting structure were averaged and error bars were calculated by taking the SE. The differences in distributions of the two states were then quantified by calculating the area between the error bars. Because the area under each distribution is 1, the difference ranges from 0 (totally overlapping error bars) to 2 (totally distinct distributions with no error).

The mean difference for each residue and nucleus type was calculated by averaging over the differences from the 17 starting structures. For amide nitrogens, amide protons, and the methyl carbons of Val residues, these differences are represented by a single row of values shown in Fig. S4. For the methyl carbons of Ile and Leu residues, the average was taken over both the χ_1 - and χ_2 -angles, corresponding to the two rows of data shown in Fig. S4.

To determine the degree to which residues with detectable RD also showed larger distribution differences, receiver operator characteristic (ROC) curves were calculated. These curves were constructed by sorting residues by the mean distribution difference and calculating the true-positive and false-positive rates for all possible cutoffs. The area under the ROC curve was used to quantify the prediction quality, with 1 corresponding to a perfect prediction and 0.5 corresponding to a random prediction.

Optimizing a Single Collective Mode to Explain the RD Data. Using the protocol described above, one can then investigate how well individual PCA modes explain the RD data, with the goal of identifying a collective motion that represents a reaction coordinate along which ubiquitin moves on the microsecond time scale. We reasoned that an optimized linear combination of PCA modes might explain the RD data better than any single PCA mode. To construct a vector of weights for this linear combination of PCs, we used a two-step procedure. In the first step, the magnitudes of the weights were

assigned. For each of the first 20 previously determined PCA modes (10), the mean ROC curve value was calculated. The mode with the highest mean area was assigned a magnitude of 1, the mode with the lowest mean area was assigned a magnitude of 0, and all other modes were assigned magnitudes by linear interpolation between those values. To normalize differences in variance captured by the modes, the magnitudes were then divided by the corresponding eigenvalues. In the second step, the signs of the weights were assigned. The mode with the highest weight was given a positive sign. The remaining weights were assigned with a greedy algorithm in which modes with successively lower weights were added one at a time with whichever sign gave the highest average ROC curve area.

Cross-Validation of the Optimization Procedure. To determine whether the optimized collective mode could predict the observation of RD in residues excluded from training, we used a “leave 20% out” cross-validation procedure. Before optimization, a randomly chosen testing set of 20% of the positive (RD observed) and 20% of the negative (RD not observed) residues was excluded for each type of nuclei. The optimization procedure was then performed using the remaining 80% of residues. The small size of the testing set led to significant variance in the mean ROC curve area for different testing sets. Therefore, we repeated the cross-validation procedure 2,500 times to yield a mean overall ROC curve area of 0.622 ± 0.003 , compared with a mean overall ROC curve area of 0.84 without cross-validation.

To estimate the statistical significance of observing that value over the background distribution of random ROC curve areas (usually assumed to average around 0.5), we repeated the cross-validation scheme with 1,000 sets of shuffled experimental data. Residues were shuffled within groups, with the groups defined by the availability of RD data. For instance, residues with amide nitrogen, amide proton, and methyl carbon data were shuffled together in one group, whereas residues with only amide nitrogen and proton data but no methyl carbon data were shuffled in a different group. For each set of shuffled experimental data, the cross-validation procedure was performed 50 times. The resulting distribution of mean ROC curve areas is shown in Fig. S3. This distribution indicates that the probability of observing a ROC curve area better than 0.622 at random is 0.027, making it unlikely that the predictive accuracy of the model is observed by chance.

Generation of Consensus Weights. The set of weights determined during the cross-validation procedure (using the unshuffled data) was rescored with the complete set of experimental data. The resulting distribution of ROC areas is shown in Fig. S3A (black line). Within that distribution, a secondary population of high ROC areas was observed. To determine a consensus vector for that set of weights, a biased PCA was performed. Before consensus PCA, all weights were multiplied by the corresponding eigenvalues from the original PCA (the same as those eigenvalues used in the first step of the optimization procedure above). A weighted covariance matrix was then calculated without centering (i.e., assuming a mean of 0 for each weight). Given a vector of mean ROC areas (A) and the vector of weights (W), the covariance matrix was calculated with the formula $W_i = (A_i - \min(A))^{1.5}$. The distribution of ROC areas reweighted with that vector is shown in Fig. S3B (blue line). After eigendecomposition of the covariance matrix, the eigenvector with the highest eigenvalue was selected. The consensus set of weights was determined by normalizing that eigenvector through division by the original PCA eigenvalues. The model produced with these weights was termed the RD fit MD mode and is different from the peptide fit PDB mode described below.

To determine whether peptide flipping would also be seen if a different set of MD trajectories were used, we repeated the fitting procedure with snapshots from the dominant state of the CHARMM22* MD trajectory (22) (Fig. S6). The resulting mode also showed peptide flipping as a prominent feature and significant similarities in per-atom magnitudes (Pearson’s product moment correlation coefficient: $P = 1.4 \times 10^{-5}$; as in Fig. S13A) and intermode dot products (Wilcoxon signed rank: $P = 9.3 \times 10^{-7}$; as in Fig. S13B) to the RD fit MD mode trained with the AMBER ff99SB trajectories.

Analysis of Peptide Flipping in PDB Structures. We started with a set of 122 PDB crystal structures having 370 distinct ubiquitin backbone conformations for residues 1–70 (taking into account multiple copies within the asymmetrical unit and alternate models). Using data from Uppsala Electron-Density Server (39), we manually inspected the region around the D52-G53 peptide bond for each structure to check whether its conformation could be unambiguously assigned. The electron density of the E24 side chain was used as evidence for either an NH-out (Fig. 2A) or NH-in (Fig. 2B) hydrogen bond network. A resolution cutoff of 2.4 Å best discriminated between the conformations that we thought could or could not be assigned. To avoid bias, we then ignored the manual inspection and only analyzed structures having

a resolution $<2.4 \text{ \AA}$, which yielded a set of 70 PDB structures and 217 distinct ubiquitin conformations.

From these structures, we extracted all nonubiquitin sequences, which were clustered by the \log_{10} of their BLAST E-values and divided into groups using a \log_{10} cutoff of -10 , such that pairs of sequences with \log_{10} E-values less than -10 were grouped together. For every PDB structure, we determined the fraction of ubiquitin structures having an NH-out peptide conformation. The largest group having no NH-out conformations was the USP family of deubiquitinases. In subsequent structural analysis using this dataset, individual ubiquitin conformations were weighted such that the total weight from all conformations in a given PDB structure was the same as the total weight from any other PDB structure.

PLS FMA. A residue from ubiquitin (PDB ID code 3MHS chain D) was selected for PLS FMA (25, 26) if any of its atoms was within 5 \AA of a USP (PDB ID code 3MHS chain A) or if both of its adjacent residues were within 5 \AA of the USP. This selection included the following 36 residues: Q2–T14, K33–P37, Q40–Q49, and K63–V70. The N, $C\alpha$, and C backbone coordinates were used for training following subtraction of the mean coordinate values. NH-in ubiquitin conformations were assigned a value of 0, and NH-out conformations were assigned a value of 1.

To determine whether these coordinates could be used to predict the peptide bond conformation, we used complete twofold cross-validation. We restricted the randomized cross-validation groups such that all of the conformations from a given PDB structure or structure group (Fig. S11B) were restricted to being entirely within a single cross-validation group. Cross-validation was repeated 100 times with 1–40 PLS components, and the predictions were evaluated with ROC areas. The best median ROC curve area was found with five PLS components. After cross-validation, the model was retrained (with five PLS components) using all structures except the structures from USP deubiquitinases. This model, which was restricted to 36

residues, was termed the peptide fit PDB mode. To determine if the resolution of the structures had an effect on the mode, we repeated the training procedure with a resolution cutoff of 2.0 \AA (136 distinct ubiquitin conformations vs. 217 at 2.4 \AA). The resulting mode showed significant similarities in per-atom magnitudes (Pearson's product moment correlation coefficient: $P = 7.6 \times 10^{-7}$; as in Fig. S13A) and intermode dot products (Wilcoxon signed rank: $P = 3.1 \times 10^{-16}$; as in Fig. S13B) to the peptide fit PDB mode trained with a cutoff of 2.4 \AA . Therefore, the choice of cutoff did not have a large impact on the PDB-derived mode.

Rosetta Structural Modeling. To determine whether the NH-out conformations showed more steric clashes with USP than NH-in conformations, we used Rosetta with the Talaris2013 score function to rebuild ubiquitin side chains in the context of a high-resolution USP2 structure bound to ubiquitin (1.26 \AA , 3NHE). First, each of the generated ubiquitin conformations was placed into the USP2 binding site. Next, RosettaScripts (40) was used to repack and then apply four cycles of rotamer trial minimization to all ubiquitin residues and all USP2 residues whose side chains were within 5 \AA of ubiquitin. This procedure was repeated 10 times per conformation. PyRosetta (41) was then used to extract intermolecular repulsive energies between ubiquitin and USP2. Because the role of the $\beta 1$ – $\beta 2$ loop (residues 8–10) in binding has been previously characterized (10), we excluded the repulsive energies from that loop. The lowest of the 10 repulsive energies for each ubiquitin conformation were then used for analysis.

ACKNOWLEDGMENTS. We thank Nathan Cook, Donna Arndt-Jovin, and Thomas Jovin for assistance with fluorescence measurements. We also thank Monica Sundd for the chemical shift assignments for the E24A and G53A mutants. This work was supported by the Max Planck Society, the European Union (European Research Council Grant Agreement 233227 to C.G.), and the Alexander von Humboldt Foundation (C.A.S.).

- Perutz MF (1970) Stereochemistry of cooperative effects in haemoglobin. *Nature* 228(5273):726–739.
- Watson LC, et al. (2013) The glucocorticoid receptor dimer interface allosterically transmits sequence-specific DNA signals. *Nat Struct Mol Biol* 20(7):876–883.
- Perica T, et al. (2014) Evolution of oligomeric state through allosteric pathways that mimic ligand binding. *Science* 346(6216):1254–1256.
- Flock T, et al. (2015) Universal allosteric mechanism for $G\alpha$ activation by GPCRs. *Nature* 524(7564):173–179.
- Lange OF, et al. (2008) Recognition dynamics up to microseconds revealed from an RDC-derived ubiquitin ensemble in solution. *Science* 320(5882):1471–1475.
- De Simone A, Richter B, Salvatella X, Vendruscolo M (2009) Toward an accurate determination of free energy landscapes in solution states of proteins. *J Am Chem Soc* 131(11):3810–3811.
- Markwick PR, et al. (2009) Toward a unified representation of protein structural dynamics in solution. *J Am Chem Soc* 131(46):16968–16975.
- Vögeli B, et al. (2009) Exact distances and internal dynamics of perdeuterated ubiquitin from NOE buildups. *J Am Chem Soc* 131(47):17215–17225.
- Fenwick RB, et al. (2011) Weak long-range correlated motions in a surface patch of ubiquitin involved in molecular recognition. *J Am Chem Soc* 133(27):10336–10339.
- Peters JH, de Groot BL (2012) Ubiquitin dynamics in complexes reveal molecular recognition mechanisms beyond induced fit and conformational selection. *PLoS Comput Biol* 8(10):e1002704.
- Massi F, Grey MJ, Palmer AG, 3rd (2005) Microsecond timescale backbone conformational dynamics in ubiquitin studied with NMR R1rho relaxation experiments. *Protein Sci* 14(3):735–742.
- Ban D, et al. (2012) Exceeding the limit of dynamics studies on biomolecules using high spin-lock field strengths with a cryogenically cooled probehead. *J Magn Reson* 221:1–4.
- Smith CA, et al. (2015) Population shuffling of protein conformations. *Angew Chem Int Ed Engl* 54(1):207–210.
- Ban D, et al. (2011) Kinetics of conformational sampling in ubiquitin. *Angew Chem Int Ed Engl* 50(48):11437–11440.
- Bouvignies G, et al. (2011) Solution structure of a minor and transiently formed state of a T4 lysozyme mutant. *Nature* 477(7362):111–114.
- Neudecker P, et al. (2012) Structure of an intermediate state in protein folding and aggregation. *Science* 336(6079):362–366.
- Vijay-Kumar S, Bugg CE, Cook WJ (1987) Structure of ubiquitin refined at 1.8 \AA resolution. *J Mol Biol* 194(3):531–544.
- Huang KY, Amodeo GA, Tong L, McDermott A (2011) The structure of human ubiquitin in 2-methyl-2,4-pentanediol: A new conformational switch. *Protein Sci* 20(3):630–639.
- Sidhu A, Suroliya A, Robertson AD, Sundt M (2011) A hydrogen bond regulates slow motions in ubiquitin by modulating a β -turn flip. *J Mol Biol* 411(5):1037–1048.
- Salvi N, Ulzega S, Ferrage F, Bodenhausen G (2012) Time scales of slow motions in ubiquitin explored by heteronuclear double resonance. *J Am Chem Soc* 134(5):2481–2484.
- Ma P, et al. (2014) Probing transient conformational states of proteins by solid-state $R(1\rho)$ relaxation-dispersion NMR spectroscopy. *Angew Chem Int Ed Engl* 53(17):4312–4317.
- Piana S, Lindorff-Larsen K, Shaw DE (2013) Atomic-level description of ubiquitin folding. *Proc Natl Acad Sci USA* 110(15):5915–5920.
- Kitahara R, Yokoyama S, Akasaka K (2005) NMR snapshots of a fluctuating protein structure: Ubiquitin at 30 bar–3 kbar. *J Mol Biol* 347(2):277–285.
- Ermolenko DN, Dangi B, Gvritshvili A, Gronenborn AM, Makhataadze GI (2007) Elimination of the C-cap in ubiquitin structure, dynamics and thermodynamic consequences. *Biophys Chem* 126(1–3):25–35.
- Hub JS, de Groot BL (2009) Detection of functional modes in protein dynamics. *PLoS Comput Biol* 5(8):e1000480.
- Krivobokova T, Briones R, Hub JS, Munk A, de Groot BL (2012) Partial least-squares functional mode analysis: Application to the membrane proteins AQP1, Aqy1, and CLC-ec1. *Biophys J* 103(4):786–796.
- Haririnia A, et al. (2008) Mutations in the hydrophobic core of ubiquitin differentially affect its recognition by receptor proteins. *J Mol Biol* 375(4):979–996.
- Zhang Y, et al. (2013) Conformational stabilization of ubiquitin yields potent and selective inhibitors of USP7. *Nat Chem Biol* 9(1):51–58.
- Phillips AH, et al. (2013) Conformational dynamics control ubiquitin-deubiquitinase interactions and influence in vivo signaling. *Proc Natl Acad Sci USA* 110(28):11379–11384.
- Michielsens S, et al. (2014) A designed conformational shift to control protein binding specificity. *Angew Chem Int Ed Engl* 53(39):10367–10371.
- Ernst A, et al. (2013) A strategy for modulation of enzymes in the ubiquitin system. *Science* 339(6119):590–595.
- Renatus M, et al. (2006) Structural basis of ubiquitin recognition by the deubiquitinating protease USP2. *Structure* 14(8):1293–1302.
- Korzhev DM, Orekhov VY, Kay LE (2005) Off-resonance $R(1\rho)$ NMR studies of exchange dynamics in proteins with low spin-lock fields: An application to a Fyn SH3 domain. *J Am Chem Soc* 127(2):713–721.
- Eichmüller C, Skrynnikov NR (2005) A new amide proton $R(1\rho)$ experiment permits accurate characterization of microsecond time-scale conformational exchange. *J Biomol NMR* 32(4):281–293.
- Ishima R, Torchia DA (2003) Extending the range of amide proton relaxation dispersion experiments in proteins using a constant-time relaxation-compensated CPMG approach. *J Biomol NMR* 25(3):243–248.
- Yip GN, Zwietering ER (2004) A phase cycle scheme that significantly suppresses offset-dependent artifacts in the $R(2)$ -CPMG 15N relaxation experiment. *J Magn Reson* 171(1):25–36.
- Long D, Liu M, Yang D (2008) Accurately Probing Slow Motions on Millisecond Timescales with a Robust NMR Relaxation Experiment. *J Am Chem Soc* 130(51):17629.
- Han B, Liu Y, Ginzinger SW, Wishart DS (2011) SHIFTX2: Significantly improved protein chemical shift prediction. *J Biomol NMR* 50(1):43–57.
- Kleywegt GJ, et al. (2004) The Uppsala electron-density server. *Acta Crystallogr D Biol Crystallogr* 60(12 Pt 1):2240–2249.
- Fleishman SJ, et al. (2011) RosettaScripts: A scripting language interface to the Rosetta macromolecular modeling suite. *PLoS One* 6(6):e20161.
- Chaudhury S, Lyskov S, Gray JJ (2010) PyRosetta: A script-based interface for implementing molecular modeling algorithms using Rosetta. *Bioinformatics* 26(5):689–691.
- Sabo TM, et al. (2014) ORIUM: Optimized RDC-based Iterative and Unified Model-free analysis. *J Biomol NMR* 58(4):287–301.

Supporting Information

Smith et al. 10.1073/pnas.1519609113

SI Methods

Sample Preparation. Perdeuterated, ^{15}N -labeled WT and mutant ubiquitin was expressed in *Escherichia coli* adapted to 100% D_2O Toronto minimal medium supplemented with D_7 -glucose as a carbon source and ^{15}N - NH_4Cl as a nitrogen source. The ubiquitin mutants E24A and E53A were generated by PCR-based, site-directed mutagenesis using the QuikChange II Kit (Agilent) following the instructions of the supplier. The catalytic core of USP2 (amino acids 259–605) was expressed and purified following published protocols (32).

NMR. The ^{15}N $R_{1\rho}$ measurements were conducted using uniformly ^{15}N -labeled ubiquitin in 90% (vol/vol) $\text{H}_2\text{O}/10\%$ (vol/vol) D_2O . The procedure used here followed previously published methods (12, 33). Field strengths were varied from 1,000 to 6,000 Hz. Rates were determined using a two-point sampling scheme in which one reference experiment was recorded without any spin-lock period and another with a spin-lock applied for 120 ms. The errors in rates were propagated from noise in the spectra. In this study, data for T14, L43, and F45 were acquired, adding to the six previously measured dispersion curves (Fig. S1A).

The ^1H $R_{1\rho}$ was collected using a U- ^{15}N -labeled sample of perdeuterated ubiquitin in 90% (vol/vol) $\text{H}_2\text{O}/10\%$ (vol/vol) D_2O . For the measurement of ^1H $R_{1\rho}$, the experiments used follow previous methods (34). Spin-lock frequencies were varied from 1,000–10,000 Hz (277 K for WT) or 27,000 Hz (other temperatures and mutants), and were calibrated by measuring ^1H 90° pulse lengths at their corresponding power levels. Field strengths and offsets were chosen such that tilt angles of $\sim 35^\circ$ were used for all points to minimize the nuclear Overhauser effect (NOE) and rotating frame nuclear Overhauser effects (ROE) that can lead to pseudodispersion profiles (34). The experiments were carried out in an interleaved fashion, where the used delay, field strength, and offset were randomly varied. With the current experimental parameters, the overall change in the temperature was less than 1 K. Relaxation rates were determined using a three-point sampling scheme with spin-lock relaxation delays of 5, 65, and 125 ms. Rate errors were estimated using residuals from the three-point fits. Mean $R_{1\rho}$ and ω_{eff} (effective radio frequency field) values were determined using equations 5 and 6, respectively, from the study by Eichmüller and Skrynnikov (34). For each experiment, 56–188 (indirect dimension) and 1,024 (direct dimension) complex points were acquired. Four transients for each increment were collected with recycle delays of 2.3 s (277 K for WT) or 2 s (other temperatures and mutants), yielding a total experiment time of 17–58 min per data point. For E24 and G53 RD curves acquired at 308 K, the sweep width was increased from 23.5 ppm (used in other experiments) to 49.3 ppm, and a six-point sampling scheme was used with spin-lock relaxation delays of 5, 14, 23, 32, 41, and 50 ms. All ^1H experiments were conducted on a Bruker spectrometer operating at a ^1H frequency of 600 MHz.

The ^1H Carr–Purcell–Meiboom–Gill (CPMG) measurements were conducted on a U- ^{15}N and U- ^2H selectively ^{13}C -labeled (CHD_2) sample of perdeuterated ubiquitin in 90% (vol/vol) $\text{H}_2\text{O}/10\%$ (vol/vol) D_2O . The sample was loaded in nine capillaries placed into a 5-mm sample tube similar to a previously published method (14). Supercooled CPMG experiments were acquired at 262 K using a relaxation compensated approach with the CPMG period following t_1 evolution (35) and phase cycling of the refocusing pulses (36, 37). The CPMG frequency (ν_{CPMG}) was varied from 211 to 2,526 Hz during a constant time period (T_{CP}) of 19 ms. For each experiment, 128 (indirect dimension) and

1,024 (direct dimension) complex points were acquired with a recycle delay of 1 s. For the CPMG experiments, 60 transients were collected for a total experiment time of 315 min per ν_{CPMG} point. For the reference experiment without the CPMG block, eight transients were collected for a total experiment time of 45 min. Rate errors were propagated from spectral noise. Effective relaxation rates ($R_{2,\text{eff}}$) were fit assuming fast exchange using the following formula:

$$R_{2,\text{eff}} = R_2 + \Phi_{\text{ex}}\tau_{\text{ex}} \left(1 - 4\nu_{\text{CPMG}}\tau_{\text{ex}} \tanh \frac{1}{4\nu_{\text{CPMG}}\tau_{\text{ex}}} \right).$$

NMR data processing and peak quantification were done with NMRPipe. Peak intensities for E24 and G53 at 308 K were calculated by taking the maximum spectral intensity in a region around the peak positions. $R_{1\rho}$ parameter fitting, error estimation, and determination of significant amounts of dispersion were done as previously described (13). CPMG data were processed in the same manner.

Optimizing a Single Collective Mode to Explain the RD Data. We also tested a third step in which the resulting weights were further refined using Nelder–Mead optimization. Although this technique produced higher ROC curve areas for the training data, it did not produce better ROC curves using the cross-validation procedure described in *Methods, Cross-Validation of the Optimization Procedure*. Therefore, we did not use this procedure in a final determination of optimized weights. Using the same cross-validation scheme, we determined that the optimal number of PCA modes to include in the optimization was 20. The top 20 eigenvectors covered 78% of the variance and 37% of the SD (i.e., atomic displacement) in the underlying coordinates.

Clustering RD Fit MD Mode into Semirigid Bodies. To identify a set of semirigid bodies in the RD fit MD mode, residues were first clustered into contiguous segments along the amino acid sequence and then clustered into discontinuous groups of segments. Backbone rmsds between the minimum and maximum projections were used for clustering. For contiguous segment clustering, residues were initially put into single-residue segments. Using a greedy algorithm, the pairs of adjacent segments having the lowest combined rmsd were successively merged. A cutoff of 0.35 Å was used to create 11 contiguous segments for group clustering. Clustering of these segments into discontinuous groups was done with the same greedy algorithm, except that merged groups were no longer required to be adjacent in sequence. A cutoff of 0.7 Å was used to create four rigid bodies.

Analysis of Peptide Flipping in MD Trajectories. For every snapshot of the 100-ns AMBER ff99SB MD trajectories (10) or the 1-ms CHARMM22* MD trajectory (22), we calculated the ψ -backbone dihedral angle of D52 and the ϕ -backbone dihedral angle of G53. To ensure that structural transitions did not wrap around this periodic ψ/ϕ -space, the angles were normalized in the following manner. First, both angles were mapped onto the range 0–360°. Second, for any ψ_i/ϕ_i -pair whose sum was greater than 350°, ψ_i was set to $\psi_i - 360$. Under this normalization, $\psi_i - \phi_i$ is centered around 80° in the NH-in conformation and -320° in the NH-out conformation.

For the CHARMM22* trajectory, the alternate states were identified by inspection of the rmsds of residues 51–53 (alternate state 1) and residues 31–41 (alternate state 2). Q-factors were

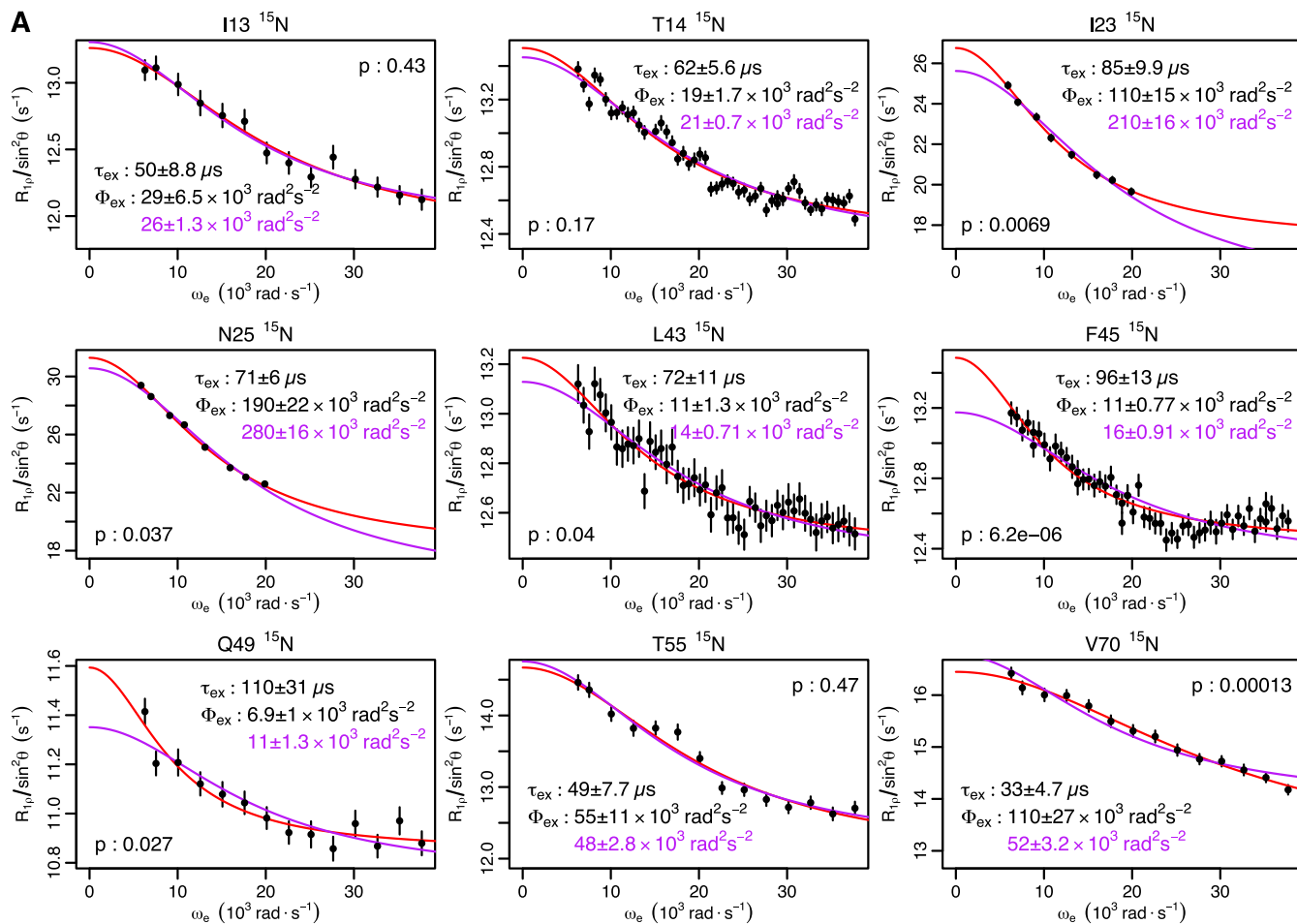


Fig. S1. (Continued)

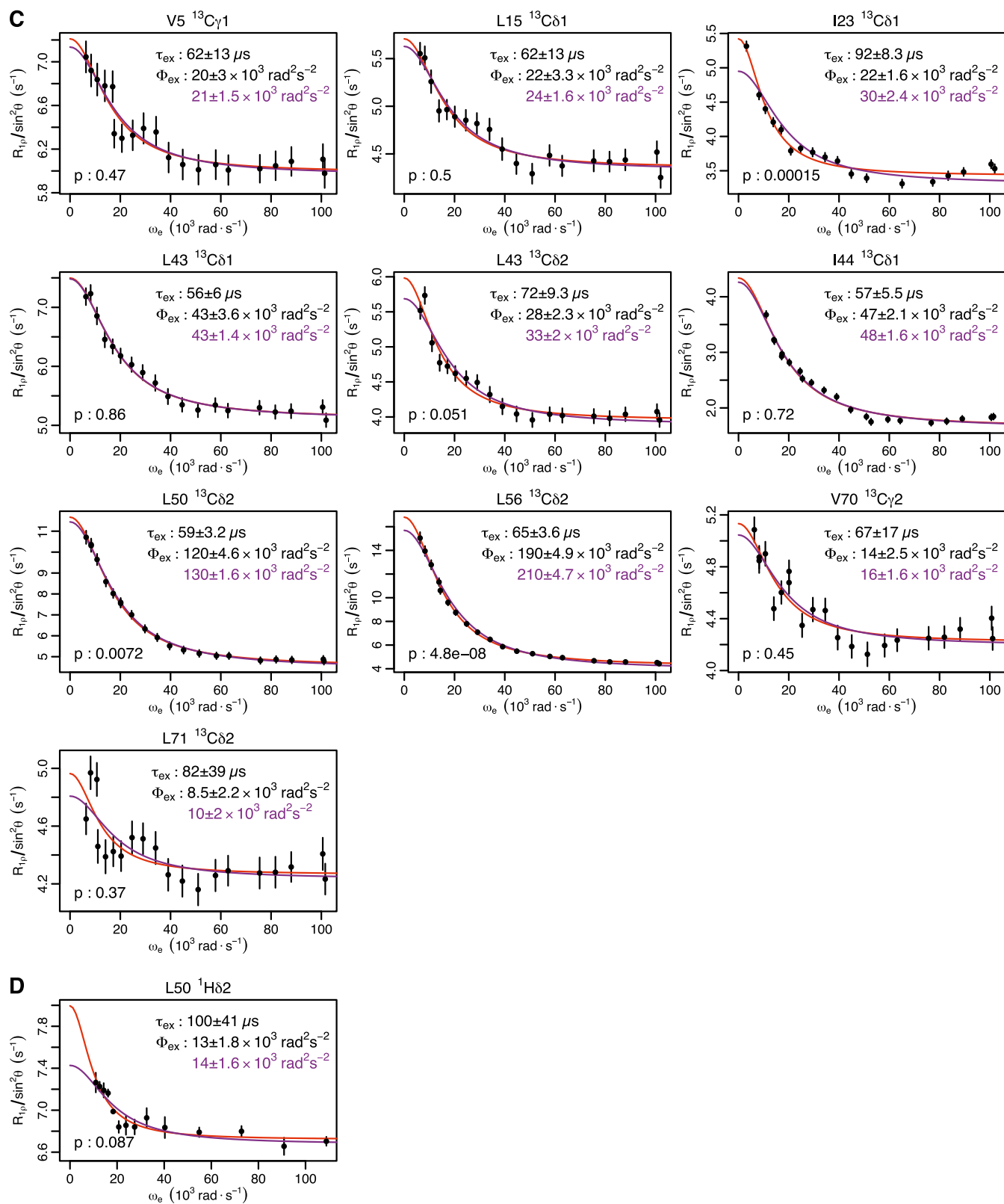


Fig. S1. Ubiquitin $R_{1\rho}$ data at 277 K. Individual fits are shown in red, with the parameters shown in black. Global fits with a single τ_{ex} (55 μs) are shown, along with the corresponding Φ_{ex} in purple. F test P values between fits are also shown. (A) Backbone ^{15}N : T14, L43, and F45 are from this study. I23 and N25 are from previous work (14). I13, Q49, T55, and V70 are from previous work (12). (B) Backbone ^1H from this study. (C) Methyl ^{13}C from previous work (13). (D) Methyl ^1H from previous work (13).

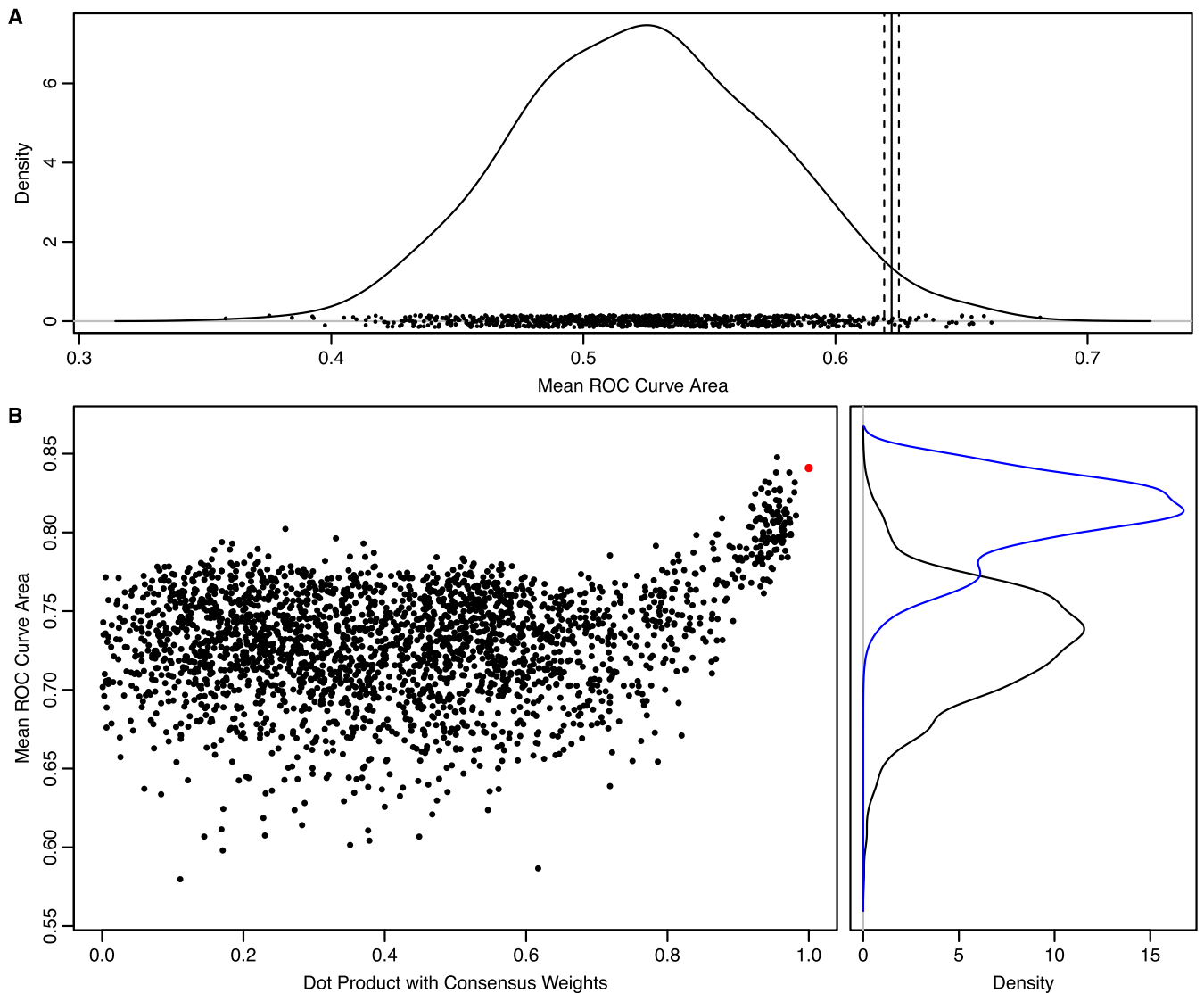


Fig. S3. Cross-validation of RD fit MD mode fitting. (A) Distribution of cross-validated mean ROC curve areas for shuffled experimental RD data. The distribution is derived using kernel density estimation with a Gaussian smoothing kernel having an SD equal to the average SE of the underlying data points (0.015). The underlying data points are shown at the base of the plot. The mean ROC curve area for unshuffled experimental data is shown as a solid vertical line, along with the associated SE (dashed vertical lines). The probability of observing a shuffled value larger than the unshuffled value is 0.027. (B) Rescoring of the different weight vectors derived from the cross-validation runs using the full set of experimental data (*Left*, black points) produces a multimodal distribution with a secondary peak having a higher mean ROC curve area (*Right*, black curve). Consensus weights were determined using PCA with a weighted covariance matrix strongly biased toward points in the secondary peak. The distribution of mean ROC curve areas using those weights is shown in blue. The consensus weights produce a higher mean ROC curve area (red point) than all but one of the cross-validation weights. The single best set of cross-validation weights is very similar to the consensus weights. The differences between the consensus weights and the different cross-validation weights are shown using the absolute value of the dot product of the respective vectors. This plot shows strong funnel-like behavior (upside down because higher values are better), suggesting that the consensus weights are close to the global minimum of the optimization landscape.

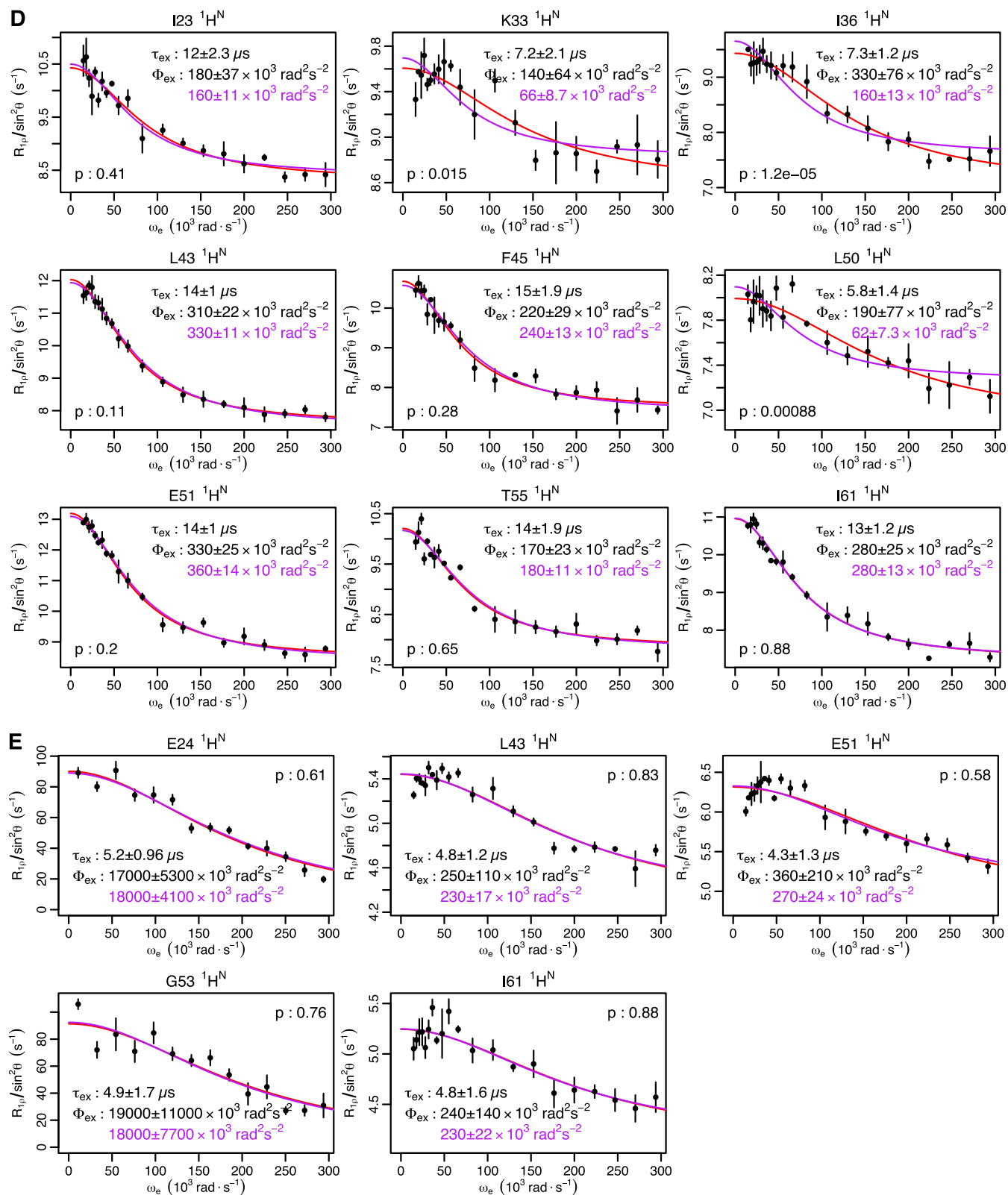


Fig. S7. Ubiquitin CPMG and $R_{1\rho}$ data at other temperatures. Individual fits are shown in red, with the parameters shown in black. Global fits with a single τ_{ex} value are shown, along with the corresponding Φ_{ex} value in purple. *F* test *P* values between fits are also shown. (A) Backbone $^1\text{H}^{\text{N}}$ CPMG at 262 K (global $\tau_{ex} = 150 \mu\text{s}$). (B) Backbone $^1\text{H}^{\text{N}}$ $R_{1\rho}$ at 282 K (global $\tau_{ex} = 29 \mu\text{s}$). (C) Backbone $^1\text{H}^{\text{N}}$ $R_{1\rho}$ at 287 K (global $\tau_{ex} = 20 \mu\text{s}$). (D) Backbone $^1\text{H}^{\text{N}}$ $R_{1\rho}$ at 292 K (global $\tau_{ex} = 13 \mu\text{s}$). (E) Backbone $^1\text{H}^{\text{N}}$ $R_{1\rho}$ at 308 K (global $\tau_{ex} = 5.0 \mu\text{s}$).

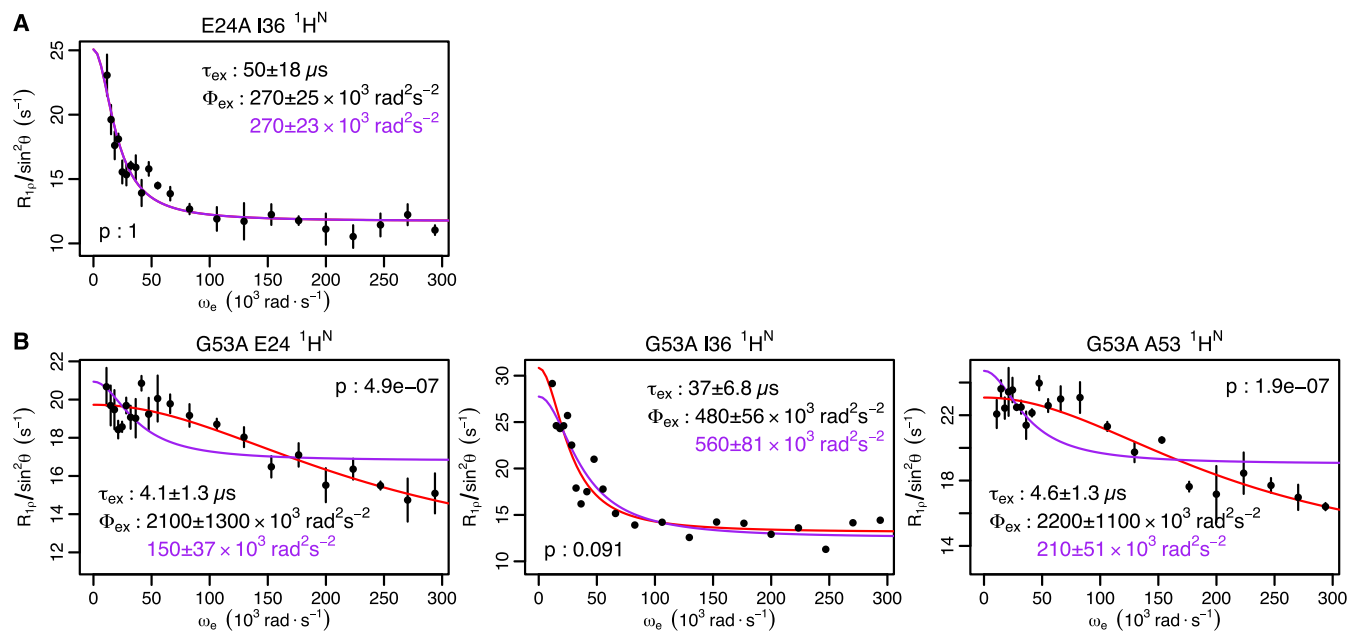


Fig. 58. Ubiquitin mutant $R_{1\rho}$ data. Individual fits are shown in red, with the parameters shown in black. Global fits with a single τ_{ex} value are shown, along with the corresponding Φ_{ex} value in purple. F test P values between fits are also shown. (A) E24A backbone $^1\text{H}^{\text{N}}$ of I36 at 277 K (global $\tau_{\text{ex}} = 50 \mu\text{s}$). (B) G53A backbone $^1\text{H}^{\text{N}}$ at 277K (global $\tau_{\text{ex}} = 27 \mu\text{s}$). Ten of 11 residues where RD is observed in WT (Fig. S1B) do not show RD in the mutants. I36 still shows RD for both mutants, suggesting it reports a different process, possibly unwinding of the α -helix that has been observed experimentally (23, 24) and in simulations (22). The I36 $^1\text{H}^{\text{N}}$ time scales are consistent for WT ($\tau_{\text{ex}} = 48 \pm 6 \mu\text{s}$) and both mutants. For the G53A mutant, the RD at E24 and A53 is about 10-fold faster than WT (55 μs). The Φ_{ex} value for these two nuclei is reduced about 10-fold over the Φ_{ex} value observed at 308 K (Fig. S7E), suggesting that the population of the NH-in state is reduced ~ 20 -fold over WT. A similar 10-fold reduction of the Φ_{ex} values observed for WT at 277 K would drop the 10 residues not observed in the G53A mutant below the detection threshold, explaining their disappearance.

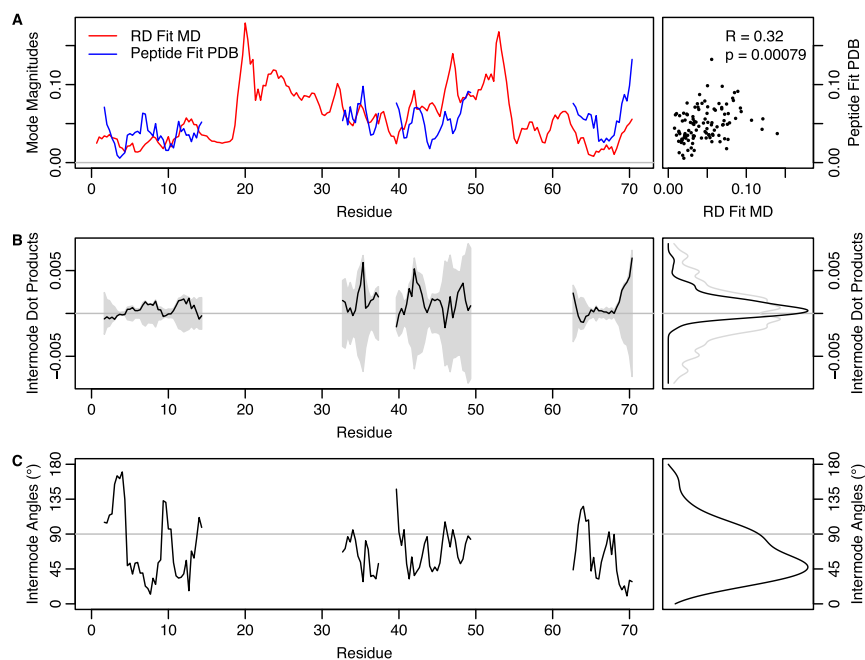
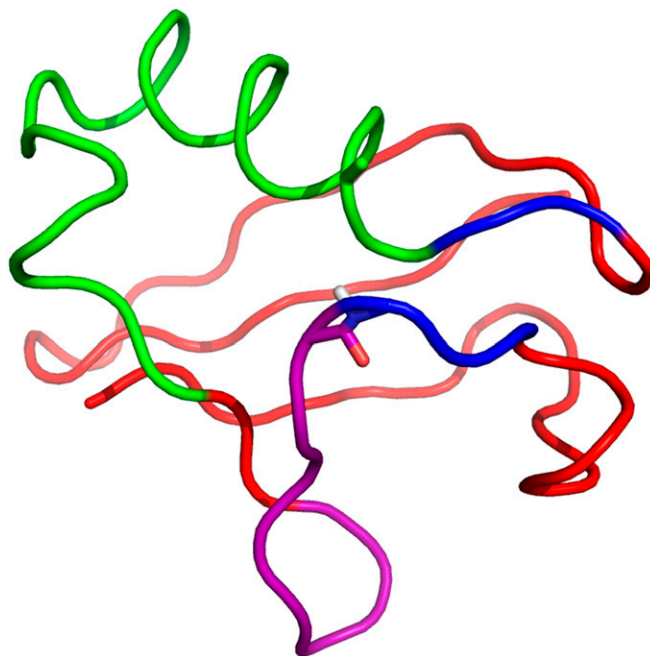
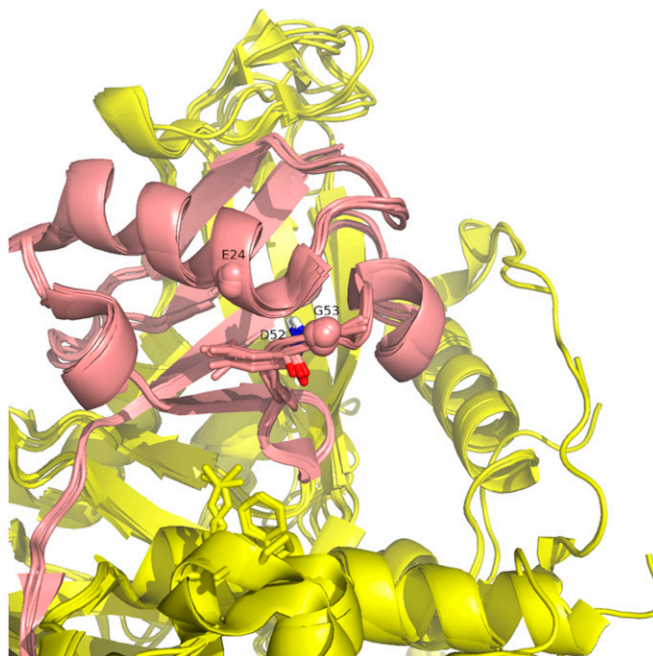


Fig. S13. RD fit MD mode and peptide fit PDB mode are similar. The magnitudes and directions of motion for every atom (backbone N, C α , C) were extracted from both the RD fit MD mode and peptide fit PDB mode. (A) Magnitudes of the RD fit MD mode (red) do coincide with magnitudes of the peptide fit PDB mode (blue). The correlation is modest ($R = 0.32$) but statistically significant ($P = 0.00079$). (B) Mostly positive (84 of 108) per-atom dot products between modes indicate that the majority of atoms move in similar directions in both modes (Wilcoxon signed rank: $P = 9.9 \times 10^{-11}$). The shaded area indicates the range of possible per-atom dot products, given the magnitudes shown in A. (C) Peak angular difference between per-atom directions of motion is $\sim 45^\circ$.



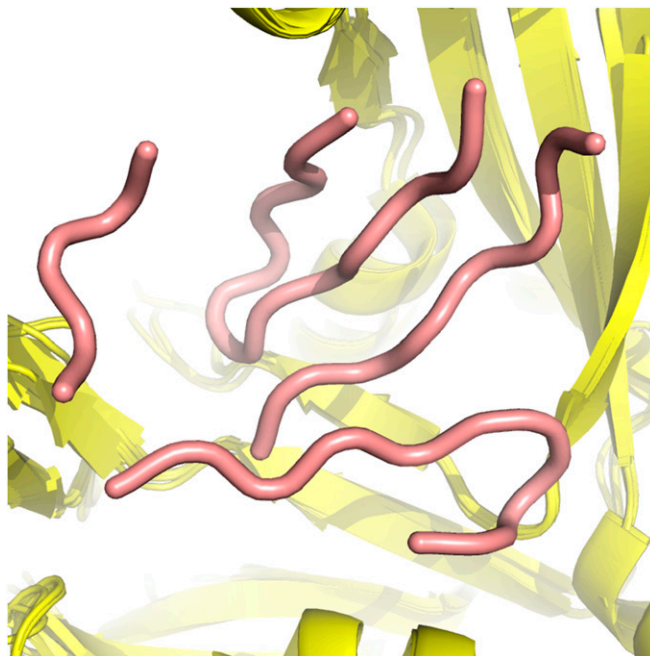
Movie S1. RD fit MD mode. Interpolation of between extremes of the RD fit MD mode is as shown in Fig. 1F.

[Movie S1](#)



Movie S2. Ubiquitin/USP complex crystal structures. Six high-resolution ($<2.4 \text{ \AA}$) ubiquitin (pink)/USP (yellow) crystal structures are shown (1NBF:C/B, 1NBF:D/A, 2HD5:B/A, 2IBI:B/A, 3MHS:D/A, and 3NHE:B/A). Ubiquitin residues D52 and G53 are shown with a stick representation. Any USP residue within 10 \AA of the D52-G53 peptide bond (colored red, white, and blue) is also shown with a stick representation. The C_{α} atoms of E24 and G53, which were mutated to Ala, are shown as spheres.

[Movie S2](#)



Movie S3. Peptide fit PDB mode. Interpolation of between extremes of the peptide fit PDB mode is as shown in Fig. 4A.

[Movie S3](#)